ARTICLE

In Situ Electrochemistry inside the TEM with Controlled Mass Transport

Received 00th January 20xx,
Accepted 00th January 20xx

DOI: 10.1039/x0xx00000x

Anne France Beker,[a] Hongyu Sun,[a] Mathilde Lemang,[a] J.Tijn van Omme,[a] Ronald G. Spruit,[a] Marien Bremmer,[b] Shibabrata Basak,[c] H.Hugo Pérez Garza,*[a]

The field of electrochemistry promises solutions for the future energy crisis and environmental deterioration by developing optimized batteries, fuel-cells and catalysts. Combined with in situ Transmission Electron Microscope (TEM), it can reveal functional and structural changes. A drawback of this relatively young field is reproducibility in controlling the liquid environment while retaining imaging and analytical capabilities. Here, a platform for in situ electrochemical studies inside the TEM with pressure-driven flow is presented, with the capability to control the flow direction and to ensure the liquid will always pass through the region of interest. As a result, the system offers the opportunity to define the mass transport and control the electric potential, giving access to the full kinetics of the redox reaction. In order to show the benefits of the system, copper dendrites are electrodeposited and show reliable electric potential control. Next, their morphology is changed by tuning the mass transport conditions. Finally, at a liquid thickness of approximately 100 nm, the diffraction pattern revealed the <1,1,1> planes of the copper crystals, indicating atomic resolution down to 2.15Å. Such control on the liquid thickness enabled elemental mapping, allowing us to distinguish the spatial distribution of different elements in liquid.

A Introduction

Global warming and using resources in a sustainable way are some of the biggest challenges of this century. Electrochemical techniques can help tackle these challenges by improving CO2 reducing technologies. Two possibilities are linked to electrochemistry: developing better energy storage and conversion (batteries, supercapacitors, fuel cells),[1–3] or designing better catalysts for a more sustainable chemical industry.[4] In both cases linking the material's morphology at the nanoscale to its functionality leads to a better fundamental understanding of the electrochemical reactions and of failure mechanisms. This helps to improve their design and efficiency, therefore lowers their costs.

Liquid Phase Transmission Electron Microscopy (LPTEM) has an important role to play, since it combines advantages of comparable techniques: the high resolution of electrochemical Scanning Tunneling Microscopy,[5] electrochemical Atomic Force Microscopy[6] and the chemical analysis toolbox of x-ray diffraction from a synchrotron source.[7] LPTEM combined with biasing electrodes shows huge promise to help solve these problems, by allowing to combine the high sensitivity of electrochemical measurements[8,9] with dynamic nanoscale imaging and chemical structure analysis in situ in one platform.

LPTEM has already provided important insights in applications like corrosion[10] or metal electrodeposition relevant to the semiconductor industry, as well as soft matter[11] and biology.[12] However, a hurdle in the electrochemical LPTEM field is to reliably control the electrical potential in liquid, therefore the heterogeneous electron transfer rate. Another equally important obstacle, is the possibility to regulate the flow and therefore the mass transport towards the reaction site. Having the capability to control these two will enable researchers to fully control the kinetics of the reaction to study.

To achieve this, we use Micro Electromechanical System (MEMS) devices acting as a sample carrier. Such device, referred to as the Nano-Cell, consists of two chips that are sandwiched together to form a sealed liquid micro-chamber[13] (Figure 1a). As opposed to other in situ liquid systems on the market that rely on a bathtub-like pocket structure to fill in the Nano-Cell (resulting in high dead volumes), the Nano-Cell has been designed to include the inlet and the outlet located on the bottom chip. The on-chip inlet and outlet are surrounded by a spacer that allows to form a closed liquid chamber upon sandwiching it with the top chip (Figure 1b). As a result, the liquid is prohibited from by-passing the chips and relying on diffusion to fill in the region of interest, as used to be the case in our first generation of systems for in situ liquid phase electron microscopy (Figure 1c) and other reported systems.[14,15] Doing in situ LPTEM experiments with systems that rely on diffusion, results in poorly defined reaction kinetics. It also hinders successfully flushing away the chemical radicals that will form due to an avoidable radiolysis process. Therefore, and in order to overcome these limitations, our next-generation in situ LPTEM system, Stream, offers the capability to independently

[a] DENSsolutions B.V., Informaticalaan 12, 2628 ZD, Delft, The Netherlands
[b] BioTop Medical, Rijnsburgerweg 10, 2333 AA, Leiden, The Netherlands
[c] Institute of Energy and Climate Research, Fundamental Electrochemistry (IEK-9), Forschungszentrum Jülich GmbH, 52425 Jülich, Germany
Electronic Supplementary Information (ESI) available: See DOI: 10.1039/x0xx00000x

control the pressure of both the inlet (up to 3000 mbar) and outlet (down to 50mbar), thus controlling the absolute pressure inside the microchamber (from 525mbar up to 1525 mbar). This generates a pressure-driven flow that ensures the liquid will reliably pass across the imaging area (Figure 1d and **Figure S4**). This pressure control also allows to manipulate the bulging of the windows and therefore the thickness of the liquid layer.[16] This has the benefit of improving the spatial resolution, enabling meaningful electron diffraction and elemental mapping in liquid. The three electrodes (working, reference and counter) located on the bottom chip allow the user to control the potential of the working electrode. The developed system empowers the user to visualize such reactions and the solid-liquid interface in real time. To illustrate this, a study of copper oxidation and reduction was carried out (since the electron transfer rate is dependent on the electric potential in liquid). Additionally, the influence of changing mass transport conditions on the morphology of copper electrodeposited at constant potential will be shown. The control over mass transport condition is very beneficial in understanding the battery electrochemistry especially at the metallic anode side.

B Design of the Nano-Cell

The Nano-Cell, inspired by our previous work on the gas-heating system,[17] is based on a dual chip concept. Since many experiments require dealing with samples that cannot be flown in from outside(e.g. lamellas), avoiding a monolithic Nano-Cell comes as the best option. Furthermore, having the capability to open up the cell enables the user to do localized surface functionalization before the experiment or post mortem analysis after the experiment.

In order to mimic a typical electrochemical cell, the Nano-Cell was designed to contain a three electrodes configuration:

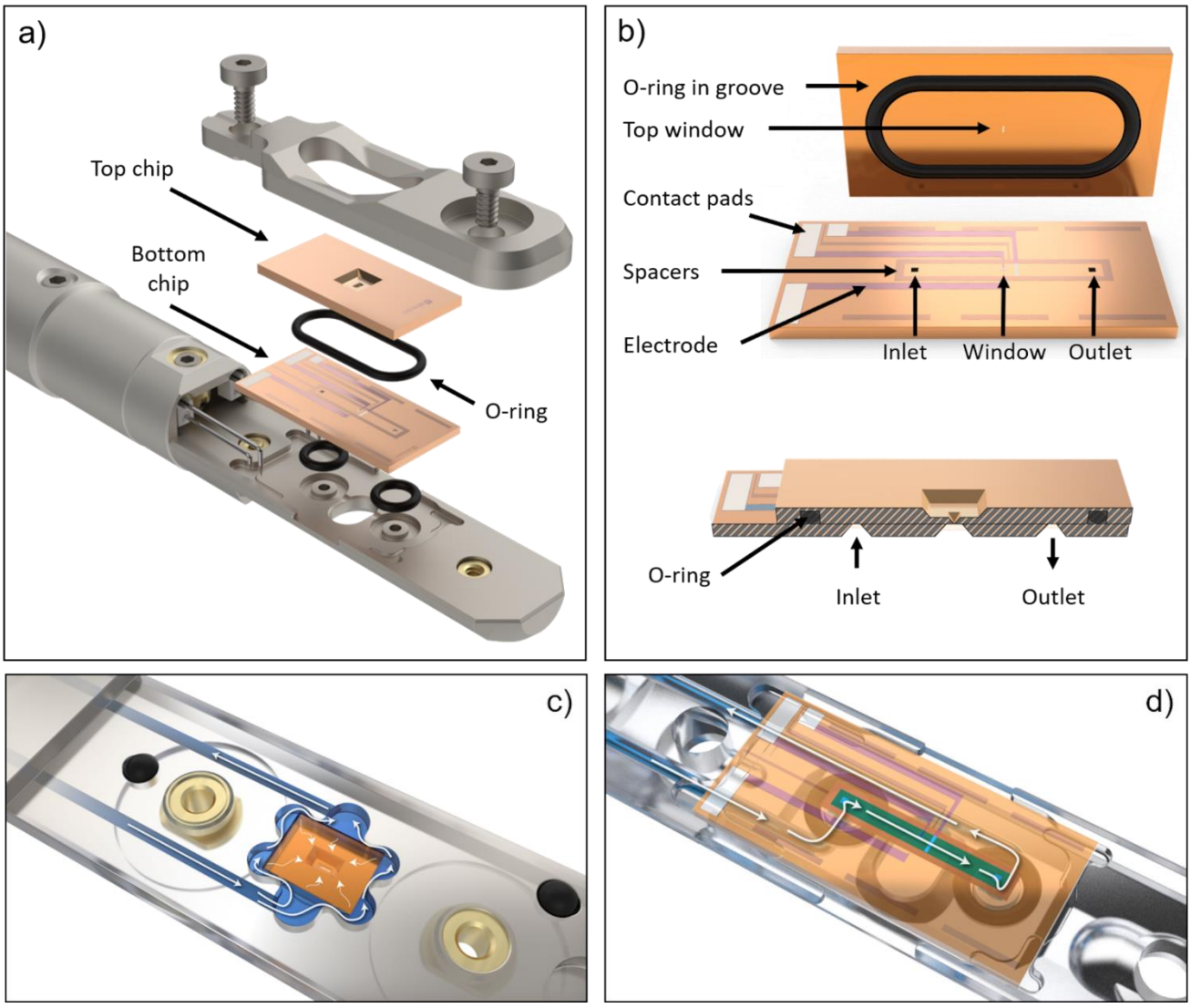

Figure 1. The Stream Liquid Biasing System. a) The Nano-Cell, relying on a dual chip concept, is mounted in the EDS compatible tip. b) The top chip, which contains a groove for an o-ring to seal the cell, has a window that is orthogonal to the bottom one. The user can independently set the pressure at the on-chip inlet and outlet, defining the absolute pressure inside of the microfluidic chamber. c) Unlike our first system for liquid microscopy (shown here for comparative purposes) and other reported systems which suffer from considerable dead volumes due to a constant by-passing effect of the windows and poor reliability on the fluidic control, d) the Stream system results in a pressure-driven flow that ensures control over the liquid passing over the window.

working electrode (WE), reference electrode (RE) and counter electrode (CE). The three electrodes are connected to a potentiostat that applies voltage between the working electrode and the reference electrode, while measuring the current flow between the working electrode and the counter electrode. Since these electrodes are immersed in a solution containing ions (electrolyte), their geometry and positioning plays an important role. The design has been supported using finite element analysis simulations.

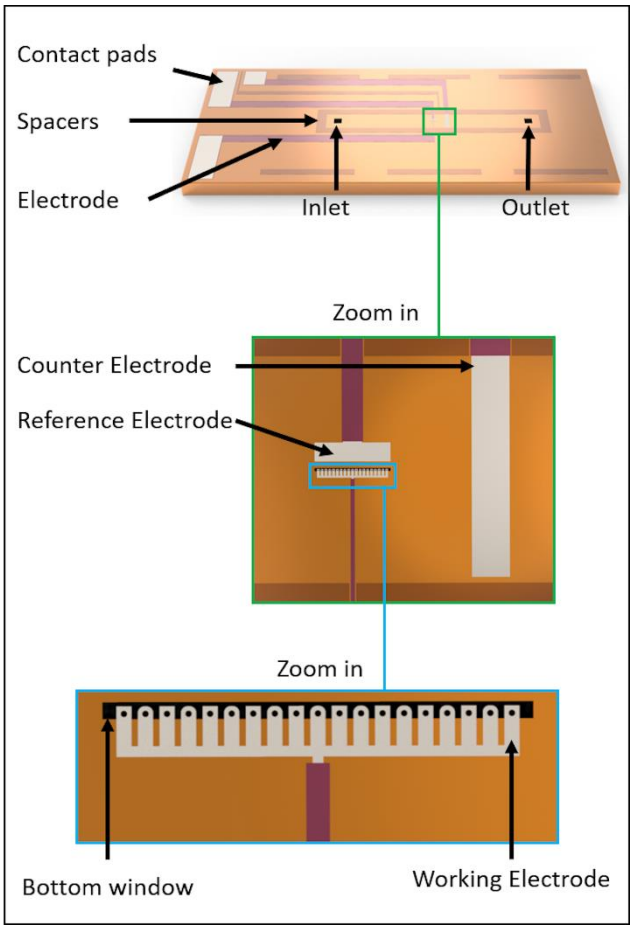

Figure 2. Architecture of the Nano-Cell. The bottom chip contains the three electrodes to perform the electrochemical experiments. The working electrode overlaps with the window and contains several fingers to simply the alignment process between top and bottom windows.

The WE was designed so that most of the conducting surface area is overlapping with the electron transparent window, to guarantee the highest possible viewing area. Additionally, the dimensions of the WE and its material properties (e.g. resistivity and mechanical stress level), were tuned in such way that: (1) it wouldn't limit the range of desired currents (thus making it less prone to current crowding effects or electromigration), (2) it wouldn't bring considerable mechanical stress to the electron transparent window and avoid failure (considering that the window would also be exposed to the liquid pressure, thus bulging). The final design of the electrodes is shown in Figure 2. A comb-shaped electrode was chosen, which covers the entire length of the window. Doing so increases the chances of having a suitable spot where to find and visualize the sample during the electrochemical experiment. Furthermore, the comb's teeth have alternating designs (round or sharp extremities), which result in different current densities. This enables the user to explore the influence of current density during the experiment. Finally, each branch was designed to have a circular window in the middle, which provides an increased viewing area. The aspect ratio of the window (diameter against thickness of the surrounding electrode) was chosen in such way, that even during the highest tilting angle inside the TEM, the region of interest is still illuminated. In order to allow a variety of experiments (such as battery, chemical conversion, water splitting...) can be performed using the system, it was important to ensure that the WE would have enough surface area to make it compatible with all types of samples geometry (e.g. nanoparticles, nanowires, lamellas). The design also ensures that it wouldn't get damaged during sample transfer (e.g. when welding the lamella after transferring).

The distance between electrodes is important (especially when working with electrolytes with low conductance), because the ohmic (IR) drop and response time of the system depend on the resistance between working and reference electrodes. Therefore, and in order to minimize the IR drop during electrochemical measurements, the RE and WE were designed to be at a close distance of 20 μm from one another, resulting in a more accurate electrochemical readout and higher sensitivity. The CE, on the other side, is placed at a longer distance (200 μm) and is used as an electron sink. Furthermore, the CE was designed to have a much larger surface area as compared to the WE, to accommodate any current needed for the potentiostat to control the working electrode's potential. Additionally, the CE was placed downstream from the RE and WE so any species generated at the CE's surface can be flushed away without interfering with the other two electrodes.

The surface area available for reaction, as well as the transport of reactants, radicals and products into and out of the electrodes has a major influence on the experimental results. In battery research (e.g. lithium-ion), the cycle life and energy density depend on these factors. Therefore, it is important to decrease the interfacial surface area between the metal electrode and the electrolyte in order to improve stability. To achieve this, we encapsulated with silicon nitride (SiN) all the metal electrodes except for the surface area that overlaps with the electron transparent membrane and thus the electrode area inside the microfluidic path. As mentioned before in traditional or commercially available systems for in situ liquid TEM, the chips are usually placed inside a pocket structure which acts as "bathtub". In these systems, the tubing for the inlet/outlet are interfacing with the bathtub-like pocket rather than with the chips themselves (as shown in Figure 1c). The liquid fills the bathtub-like pocket first before entering the chips, since the fluidic resistance to go around the chips is much lower than the resistance created by the small gap between top and bottom chips. This results in a bypass effect that hinders any kind of controlled microfluidics, since the liquid can enter the chips from any direction or at any given point in time by diffusion. We designed the Nano-Cell to have an integrated inlet/outlet complex. Incorporating these features on-chip allowed us to guarantee that the tubing (coming from the

holder) will be interfacing directly with the chips, ensuring that the liquid can be brought inside our Nano-Cell, thus preventing the undesired "bathtub" situation. Upon assembling the Nano-Cell, the top chip creates an enclosed microfluidic chamber, constraining the liquid to flow from inlet to outlet via the region of interest.

In order to keep the liquid layer as thin as possible, it is important to limit the thickness of the spacers to not more than a few hundred nanometers. Conventional systems typically rely on a syringe pump to introduce the liquid inside the Nano-Cell.[18–20] However, the syringe pump suffers from various problems: time delays (the pump controls only the speed of the stepper motor pushing the syringe and not the pressure) and low stability for a given flow rate. Therefore, the Stream system was designed in such way that the inlet and the outlet of the Nano-Cell are pressurized independently, thus giving the user the capability to control the absolute pressure inside the microfluidic chamber.

Since the fluidic motion is controlled based on pressure, a pressure-driven flow can be accurately set, to define the fluidic motion (static or continuous) as well as the direction and control the liquid thickness. The latter aspect is extremely important, since analytical techniques like Energy-dispersive X-ray spectroscopy (EDS), Electron Energy Loss Spectroscopy (EELS) or electron diffraction are dependent on the liquid thickness. Ideally, the liquid should be limited below the beam broadening, which is normally expected to happen around 500nm of liquid thickness.[21,22] The Nano-Cell was designed so that based on the spacer thickness and the maximum bulging of the windows (top and bottom), the thickness stays below the beam broadening threshold. Furthermore, the length and particularly the orientation of the top window are defined to enable EDS detection, since the window is facing the (side entry) detectors The top chip was designed in such way that the excess of bulk silicon was removed for higher signal collection. This, in combination with the tilting capabilities of the system (±30°) and the bulging control (for minimum liquid thickness), gives the user the possibility to do meaningful EDS detection.

In order to achieve nanometer resolution, the windows were designed to have a thickness of 50nm, to introduce as little electron scattering as possible, and yet contribute to a good stiffness for minimum possible bulging as well as safety of the microscope. Similarly, they were designed to be made of amorphous material (SiN) to prevent the superposition of periodic diffraction patterns. The finite element analysis confirmed that for this thickness and the previously described dimensions, at 1 bar pressure, each membrane would bulge to a maximum of 150nm on the whole window. That means, a maximum of 300nm in thickness contribution coming from the bulging of both windows is expected. But since the user can control the absolute pressure inside the Nano-Cell, the level of bulging can always be minimized. The spacer thickness, which is defined to be 200nm. This means one is not restricted to imaging at the corners of the window. This is important in particular for electrochemical experiments where the region of interest is on or at the edge of the electrode, rather than at the edge of a window.

C Results

A Bubble dissolution

The presence of bubbles in an electrochemical experiments can change the reaction kinetics. Therefore in an in situ experiment, it is an advantage to be able to control the presence or removal of bubbles. Here we show an example of controlled bubble dissolution, via pressure control. A bubble was created by water splitting at the working electrode's surface. By changing the Nano-Cell pressure, we are able to control the dissolution of the gas back to the liquid. As observed in Figure 3, at a lower Nano-Cell pressure(between t=8s and t=14s) the gas bubble grows bigger. When the Nano-Cell pressure is set to a higher pressure, the bubble shrinks and disappears. Movie S5 shows this process.

B Electron Energy Loss Spectroscopy (EELS) in liquid

The challenge for EELS studies in liquid is that the signal degrades in thick liquid due to multiple inelastic scattering events, i.e., the liquid thickness has a great influence on the quality of EELS data. Using the Stream system, the liquid can be flown into the microfluidic chamber, fill it and be pushed out of the window area. This process is monitored and recorded as shown in the upper panels of Figure 3. Meanwhile, EELS spectra were acquired for estimating the liquid thickness. The continuous changing of the plasmon peaks in the EELS spectra indicate the well-controlled liquid thickness. In addition, the presence of a characteristic inter-band transition [23] in Figure 4b and 4c confirm that the liquid is inside the Nano-Cell.

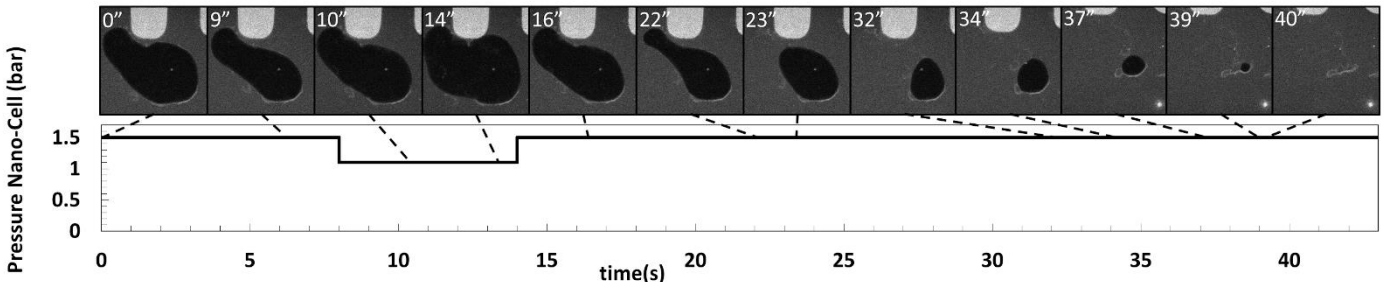

Figure 3. Time serie of stills captured in STEM mode(top) with the corresponding Nano-Cell pressure(bottom). If an unwanted bubble appears, the pressure control provided by the Stream system allows the user to dissolve the bubble by increasing the absolute pressure. The electron dose rate is 144 e- $nm^{-2}s^{-1}$.

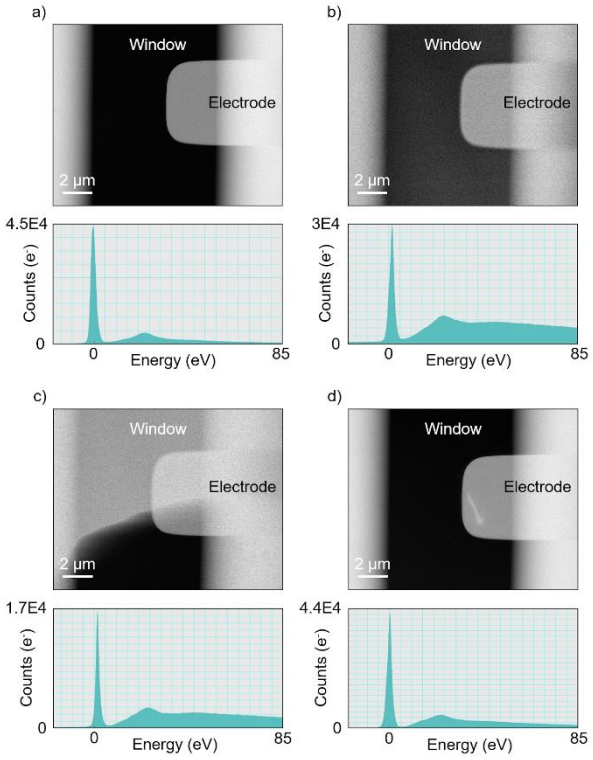

Figure 4. HAADF-STEM images of the window area of a liquid biasing Nano-Cell at different environmental conditions: (a) no liquid, (b) completely filled with liquid, (c) half evacuated and (d) no liquid. The liquid flow moving through the window area can be facilely controlled by the Stream fluidic system. Meanwhile, the liquid thickness can also be tuned in the field of view, as confirmed by the continuous changing of the plasmon peaks in the EELS spectra at the bottom of corresponding images The electron dose rate is 144 e- $nm^{-2}s^{-1}$.

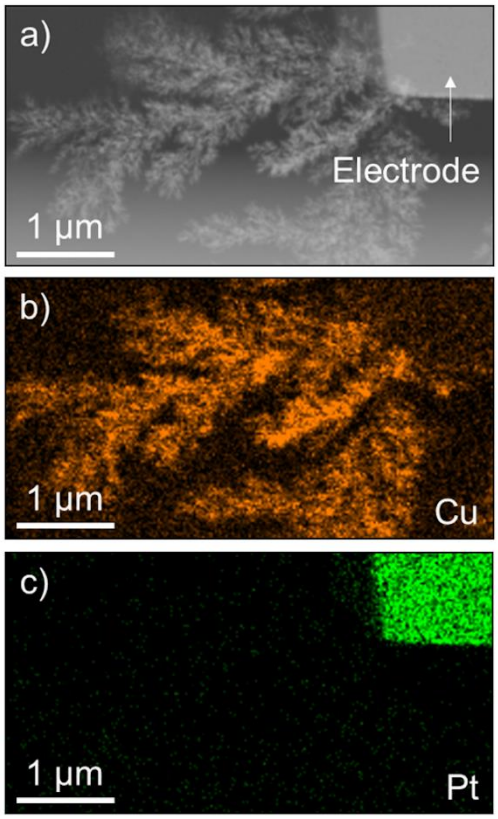

Figure 5. (a) HAADF-STEM image of Cu dendrites attached to the Pt electrode; EDX elemental mapping, showing the spatial distribution of (b) the Cu dendrites and (c) the Pt electrode in the electrolyte. The electron dose rate was kept at ~288 e- nm-2s-1 to avoid beam induced copper deposition in the liquid.

C Elemental mapping in liquid

Identifying the chemical composition and their distribution through liquid media of moderate thicknesses is important to study different applications, including nanoparticle synthesis and degradation, catalyst and electrode evolution during working reactions, chemical or electrochemical corrosion. The "Stream" holder and Nano-Cell design minimize the penumbra of the holder and the Si substrate of the chips, to avoid the shadowing of the EDX detector from the specimen. Therefore, the highest X-ray counts can be collected, making it convenient to perform valuable EDX elemental analysis in liquid. Figure 5 illustrates a secondary electron image and corresponding elemental mapping, which were taken from the Nano-Cell containing electrolyte. The STEM image (Figure 5a) shows the dendritic copper (Cu) crystals attached to the platinum (Pt) electrode. The elemental maps (Figure 5b, c) reconstructed from X-ray spectra at each imaging pixel allows mapping and identifying the two different elements (Cu and Pt) through obvious atomic number contrast. From the images, the smallest elementally resolved structure is ~25 nm.

D High resolution imaging and electron diffraction in liquid

Inelastic electron scattering dominates the interactions when the liquid is thick. Especially, the phase contrast equations are invalid when the liquid thickness is larger than ~160 nm.[22] Consequently, acquiring high resolution images and electron diffraction in dual-chip liquid cell is a challenge, although atomic scale image and electron diffraction can be achieved in graphene liquid cell with thin (from several to several tens of nanometer) liquid pockets[24] or in conventional Silicon Nitride liquid cell TEM, provided the liquid is thin enough. [23]

Benefitting from the facile control over the liquid thickness through changing inlet and outlet pressure of the Nano-Cell, we can push out the liquid and analyze a sample with atomic resolution by using the "Stream" holder. A leftover liquid layer is present which is important to keep the sample in its reaction environment. Figure 6a-b shows typical HRTEM images of the electrodeposited Cu layer in the liquid. The lattice-resolved image (Figure 6a) demonstrates the Cu layer is single crystal. The clear lattice fringe with spacing value of 2.15 Å matches very well with the (111) plane of face-centered cubic Cu (JCPDS file no. 04-0836). The capability of imaging Cu <111> diffraction means the liquid layer is not more than 100 nm in the field of view.[25]

In contrast to high resolution imaging, electron diffraction provides structural information in reciprocal space. For thick liquid layer (> 500 nm), no diffractions can be observed due to the serious scattering of the incident electron beam by the liquid. In conventional LPTEM, electron diffraction can often be

obtained by evaporating the liquid, leaving a thin liquid layer inside the liquid cell.[26]

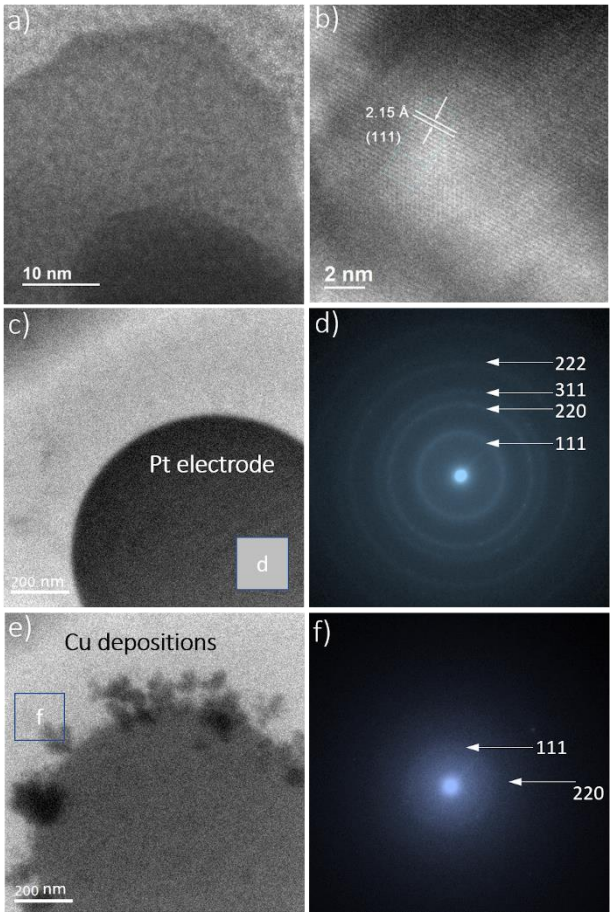

Figure 6. In situ results in 100 nm liquid a-b) in situ HRTEM images of the electrodeposited copper. TEM images of (c) the platinum electrode and (e) the copper dendrites on the electrode, and (d, f) the corresponding SAED patterns in the liquid phase. The 220 diffraction of copper crystals can be distinguished. The electron dose rate was kept at ~196 e- nm-2s-1 to avoid beam induced copper deposition in the liquid.

Similarly, the "Stream" system enabled us to acquire the diffractions in liquid environment (liquid thickness down to 100 nm after pushing out the liquid). Figure 6 c-f displays TEM images and corresponding selected area electron diffraction (SAED) patterns on the Pt electrode and the Cu dendrites on the electrode. The Pt electrode (Figure 6c) was firstly imaged with a thin liquid layer, which was formed due to the remaining water inside the tubing set. After flowing the electrolyte and growing the Cu dendrites, the liquid thickness was tuned by applying different inlet/outlet pressure. In this case, two diffractions (111) and (220) of Cu crystals can be distinguished.

E In situ electrochemical growth of copper dendrites

The ex situ characterization by cyclic voltammetry of copper oxido-reduction was reproduced in situ. The holder with a mounted Nano-Cell was inserted in the TEM. The 20 mM of $CuSO_4$ and 10 mM of KH_2PO_4 solution is flowed in the Nano-Cell through the inlet presented in Figure 1. Growth and stripping of copper is completed a few times via cyclic voltammetry. The beam dose rate was adjusted to avoid beam induced copper deposition. Once again, the five cycles presented in Figure 7 are the ones obtained after stabilization of the reference electrode's potential. Cycles begin with copper reduction (I to II) that corresponds to the growth of copper dendrites as presented in Figure 7b. Then oxidation takes place (II to I) and the copper is stripped. The growth and the stripping of copper dendrites as recorded using STEM is shown in Figure 7a, for the first and the fifth cycle. The copper dendrites that are highlighted are thicker after reduction and become thinner after oxidation, corresponding in time to the current-voltage characteristic recorded. However, they do not return to their initial state. As we can see, between cycle 1 and cycle 5, the size of the dendrite highlighted in Figure 7a has increased through these 5 cycles. Thus, the reaction is not totally reversible.

This point can be examined further in Figure 7b. The cyclic voltammetry curves are highly reproducible from one cycle to another, overlapping over 5 cycles. The difference with the ex-situ experiment is small. However the in situ measurement differs somewhat from the ex situ measurement: while the amplitude of the reduction peak is similar in both cases (ex situ -37.2 nA vs in situ -36.2 nA), the amplitude of the oxidation peak is smaller (ex situ +76.7 nA vs in situ + 38.4 nA), which might explain why not all the copper is stripped during the oxidation. The full 5 cycles can be seen in Movie S6.

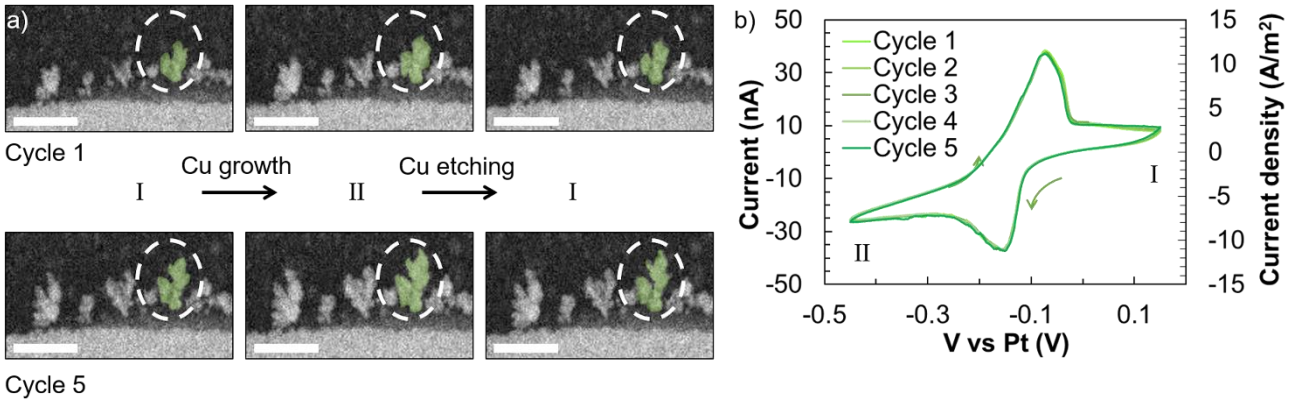

Figure 7. a) STEM imaging of the growth (I => II) and the strippinga (II => I) of copper dendrites during the first and the fifth cycles of in situ cyclic voltammetry. Scalebars are 500 nm. b) oxidation and reduction of the dendrites with cyclic voltammetry measurements for five consecutive cycles. Scan rate = 100 mV.s^{-1}. The electrolyte is: 20 mM CuSO4 + 10 mM KH2PO4.

F Mass transport control: copper morphology control

In order to show the efficiency of the flow control, two consecutive measurements were ran while a movie was recorded in STEM mode at the same position on the working electrode.

A first chronoamperometric measurement was performed, recording the current response to a step voltage (Cottrell experiment) applied at -0.2V without flow for 50 seconds (**Figure 8**). A simultaneous STEM movie was recorded at x7000 magnification. The electrode was cleaned in between the measurements (the deposited copper was stripped and electrolyte replenished).

A second chronoamperometric measurement was ran (Figure 8a) where a constant voltage of -0.3V was applied during 300 seconds. During the first 170 seconds, a constant flow of 500 nL.min^{-1} present. The current's amplitude shows a rapid increase and reaches a plateau around -190 nA. The flow is turned off from second 170 to 300. Once the flow is stopped, the current versus time plot is characteristic of a Cottrell experiment with rapid decreasing of the current's amplitude. A simultaneous STEM movie was recorded at x9900 magnification. During both measurements, the beam dose rate was adjusted to avoid beam induced copper deposition.

Figure (8b) is a comparison between the first 50 seconds in the two experiments, with and without flow, with stills from the corresponding STEM movie. The STEM images of the first measurement were reframed for comparison. A colored image of the starting situation was overlapped, to better see the evolution of the copper deposited. The movies are viewable side by side in original size (Movie S7).

D Discussion

Controlling the pressures applied to the inlet and outlet enables control over the pressure of the liquid cell itself, as an average of these two values. Therefore, this provides an additional way of dissolving unwanted gas bubbles, as shown in Figure 3. As liquids are incompressible, whereas gas is compressible, the volume of the bubble would decrease as the pressure increases. The gas in the bubble dissolves into the non-saturated liquid, obeying Henry's law.[27]

Detecting SAED patterns depends on the scattering of the incident electron beam by the liquid which is connected to the liquid thickness. Critical LPTEM characterizations are all connected to the thickness of the liquid sandwiched in the cell. The (220) diffraction plane of copper can be observed in Figure 6f and would correspond to a 1.28 Å resolution. Considering the relation between the thickness and the resolution,[25] the calculated thickness of the liquid layer is 100 nm. This is corroborated by the EELS measurements (Figure 4) with a relative thickness of $1.34\ \frac{I}{I_0}$ which leads to a liquid thickness of 105 nm. The benefits of low liquid thickness lie also in being able to use the phase contrast equations[22] that need a liquid thickness of maximum 160 nm as a valid premise. However, small thicknesses bring the question, whether the confined in situ results correlates with the ex situ results (performed in an unconfined space), to the forefront. Finally, low thicknesses in LPTEM lead to monitored high resolution imaging, diffraction (Figure 6) to provide structural information in the reciprocal space, and analytical TEM studies (EDX, EELS).

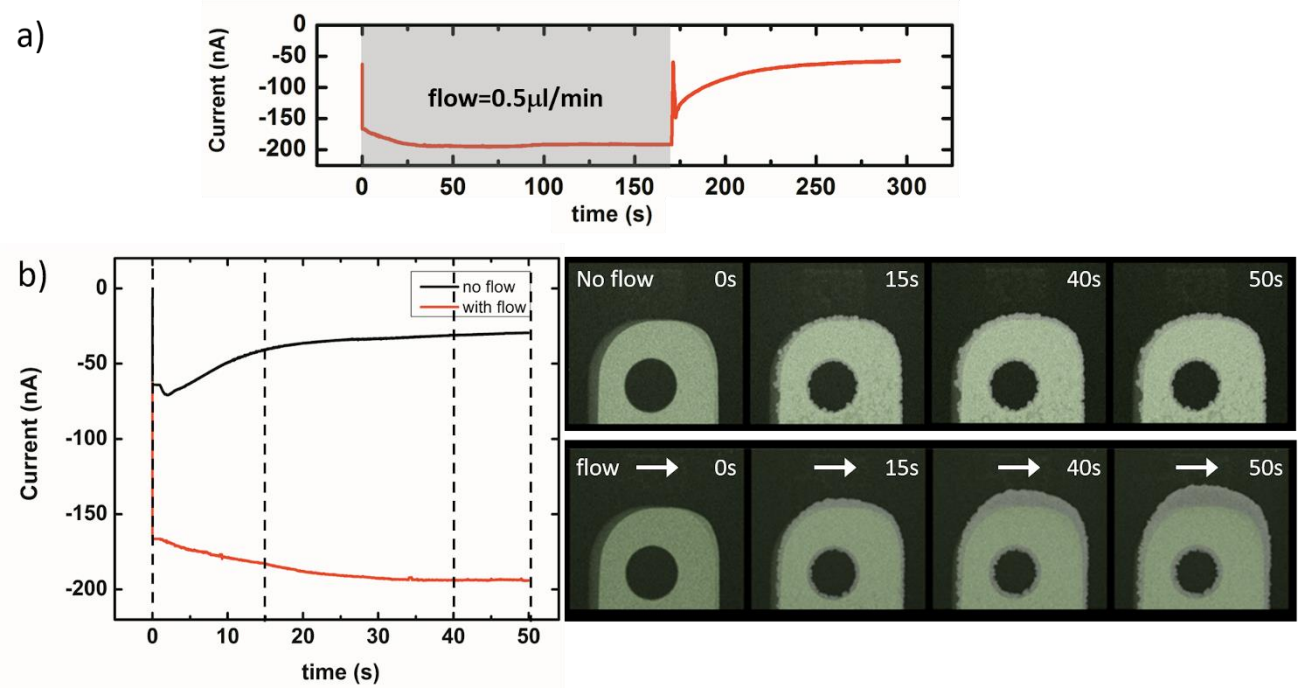

Figure 8 a) Current response to a -0.3V applied. for t=0 to t=170s, flow rate=500nL.min^{-1}. The flow is stopped at t=170s until the end. b) Comparison of the current responses with a flow rate=500nL.min^{-1} and without flow, corresponding STEM images during the measurements. In both cases, the electrolyte is: 20 mM $CuSO_4$ + 10 mM KH_2PO_4. Each STEM image dimensions is: 9.79 x 9.79 µm^2

A major nuisance when performing LPTEM experiment with an electrolyte is the influence of the electron beam and its reaction with the species composing the electrolyte. When the electron beam interacts with the copper electrolyte presented in Figure7, the availability of controlled high flows facilitates the flushing of the deposited material from the region of interest (i.e. window, sample, electrodes), as shown in Movie S4. Hence, the flow control allows to remove unwanted beam-induced species. On top of that, it is used to remove unwanted gas bubbles. The latter can be formed during a reaction as a side product, i.e. from hydrolysis. When trapped in the viewing area, the resolution improves temporarily because no more liquid is available, but their presence prevents the liquid from being observed. Therefore, control over the flow gives more control over the beam effect during experiments and provides experimental flexibility.

It is also important to highlight that the cyclic voltammetry measurements hint that the beam can have an effect and the latter should always be examined during LPTEM experiments. Once the electrolyte was flowed into the liquid cell, cyclic voltammetry was used to study the electrodeposition of copper (Figure 7). In the voltammetric plots, the potential difference between the copper oxidation peak and the copper reduction peak is 0.08 V for in situ measurements and 0.12 V for ex situ measurements. Such a difference in CV shape could be explained by a lower pH,[28] due to the electron beam irradiating the aqueous solution.

The growth of copper dendrites on the working electrode as well as their morphological development through time complies with the different peaks observed in the cyclic voltammetry profiles. Nonetheless, differences were observed between the ex situ and in situ cyclic voltammetry and they can be explained by the beam interfering with the reaction. It was observed that the size of the copper dendrites increased through these 5 cycles and that the reduction and oxidation reactions were not totally reversible. When the electron beam interacts with the electrolyte, reduction of copper ions occurs. More copper is deposited than stripped and the size of the dendrites increases. This can be due to the relatively fast voltage scan rate

Another difference between the ex situ and in situ measurements is linked to the long-term stability of the cell. It was demonstrated that the beam influences the solution, but it can also influence the electrolyte potential during the experiment. As the electrochemical setup is miniaturized and integrated on a chip, the reference electrode (RE) that is implemented here can be defined as a pseudo-reference electrode:[29] (1) the RE is immersed directly in the electrolyte instead of a reference solution and the electrode has a relatively large surface area (2) no redox couple defines the reference potential, but the latter remains stable thanks to the large area of the electrode. Nonetheless, the beam effect can impact the electrolyte and the pseudo-reference electrode. Consequently, miniaturizing a bulk reference electrode is still a challenge for all LPTEM systems, even if the current design has proved its efficiency and stability.

Finally we observed different copper growth morphology as a function of flow (Figure 8b). In the static case (no flow), we see typical decreasing current's amplitude, due to the depletion of the copper ions to be reduced in the vicinity of the electrode. In the case of the high flow, the current reaches a plateau, the reaction being constantly fed new reactants (copper ions). When the flow is turned off (Figure 8a), a similar behavior where the current amplitude decreases and reaches a plateau as in the static mode (Figure 8b). The value of the current reached when the flow is stopped is slightly more negative than for the static experiment, due to slightly higher overpotential applied, thus faster reduction. In spite of the slight difference in reducing potential applied, the flow has a higher impact on the growth, since it changes the current-time characteristic drastically (Figure 8b). If we consider the corresponding STEM movie features (Movie S7) we can witness maximum speed of copper growth at the position where the copper reduction is the most efficient: the extremity where the mass transport is highest as well the closest to the reference electrode where the ohmic drop is the lowest. Indeed, on the two parallel edges as well as the circular opening of the electrode we see slower growth happening. In a closer look, with flow the copper grows in a continuous layer while without flow the copper nuclei grow isolated not connecting in the same time frame. This, as well as the corresponding current-time characteristic, is direct proof of the flow control of the system allowing to control the kinetics of an electrochemical reaction.

This development brings added value to the liquid phase electron microscopy community. Key challenges that the LPTEM community faces are addressed: fluidic control and liquid thickness by controlling the pressure, electron beam effects by controlling the flow, experimental flexibility with live-control during the experiment, no cross-contamination thanks to the experimental workflow and reproducibility because many parameters are known and controlled during the experiment.

Conclusions

We have shown the development of the "Stream Liquid Biasing" system, for performing in situ electrochemical studies inside the TEM, with control over the mass transport. Due to its on-chip flow channel, the user can effectively and accurately control the experimental conditions; pressure, flow rate, liquid thickness, electric potential and bubbles. The system was demonstrated by showing the in situ growth of copper with different morphologies depending on the flow rate. Cyclic voltammetry measurements were stable and show a high degree of similarity between the in situ and ex situ situation. Electron diffraction, EELS and EDS analysis were used to characterize the copper dendrites and to provide additional insight into the state of the liquid inside the Nano-Cell. We believe this system holds the capability to boost the research in various application fields ranging from battery research and fuel-cells to corrosion and electrocatalysis.

Materials and methods

To demonstrate the capabilities of the system, copper dendrites were grown and characterized in situ. The bottom and the top chips were aligned following the method presented in ESI. All results shown were collected during three different sessions. The holder was leak tested and inserted in a Tecnai Osiris TEM with a Gatan US1000XP CCD camera, for the in situ electrochemical results. The EELS and EDS were acquired with a Titan 80-300 (300keV, FEI). The high resolution images and diffraction patterns were acquired with a JEOL EM 3000 F microscope.

(S)TEM imaging were carried-out to observe the "dry-state" of the Nano-Cell with a field of view comprising the working electrode. At this point, dry-state reference data is collected by EELS performed thanks to a post-column GIF 200 system, and Energy-dispersive X-ray spectroscopy (EDS) done with the help of a 4 quadrant Super X detector. The 20 mM of $CuSO_4$ and 10 mM of KH_2PO_4 solution was introduced and the "wet-state" of the Nano-Cell was imaged thanks to STEM and TEM imaging modes. This concentration of phosphate anions were added to increase the conductivity of the electrolyte, without risking precipitation of the copper without bias applied.[30] Cyclic voltammetry was carried out with a PalmSens4C™ potentiostat and a custom shielded cable to connect the working, reference and counter electrodes of the potentiostat to the holder's terminals. Copper is grown and removed on the working electrode during several cycles while recording in STEM mode. Once the copper is deposited, new EELS, EDS characterization were carried out with copper inside the viewing area. High resolution images and diffraction patterns of the grown copper dendrites were recorded in TEM imaging mode (200 keV-TEM) in water.

Conflicts of interest

A.F.B., H.S., M.L., J.T.v.O., R.G.S. and H.H.P.G. work for DENSsolutions B.V., a company manufacturing and marketing in situ TEM systems. The remaining authors have no conflicts to declare.

Acknowledgements

This work is partly financed by the WBSO program of the Netherlands, which encourages firms to spend time on research and development activities. The authors would also like to acknowledge Dr. Heiner Friedrich and Hanglong Wu from TU/Eindhoven for the fruitful discussions in related topics. Similarly, TU-Delft and EMAT are acknowledged for providing access to their microscopes.

Notes and references

.

1 M. Armand and J.-M. Tarascon, *Nature*, 2008, **451**, 652–657.
2 N. Hodnik, G. Dehm and K. J. J. Mayrhofer, *Accounts of Chemical Research*, 2016, **49**, 2015–2022.
3 B. L. Mehdi, A. Stevens, J. Qian, C. Park, W. Xu, W. A. Henderson, J.-G. Zhang, K. T. Mueller and N. D. Browning, *Scientific Reports*, 2016, **6**, 34267.
4 Y. Lum, J. E. Huang, Z. Wang, M. Luo, D.-H. Nam, W. R. Leow, B. Chen, J. Wicks, Y. C. Li, Y. Wang, C.-T. Dinh, J. Li, T.-T. Zhuang, F. Li, T.-K. Sham, D. Sinton and E. H. Sargent, *Nature Catalysis*, 2020, **3**, 14–22.
5 L. Jacobse, M. J. Rost and M. T. M. Koper, *ACS Central Science*, 2019, **5**, 1920–1928.
6 R. M. Arán-Ais, F. Scholten, S. Kunze, R. Rizo and B. Roldan Cuenya, *Nature Energy*, 2020, 1–9.
7 J. Lim, Y. Li, D. H. Alsem, H. So, S. C. Lee, P. Bai, D. A. Cogswell, X. Liu, N. Jin, Y. Yu, N. J. Salmon, D. A. Shapiro, M. Z. Bazant, T. Tyliszczak and W. C. Chueh, *Science*, 2016, **353**, 566–571.
8 S. Goines and J. E. Dick, *Journal of The Electrochemical Society*, 2020, **167**, 037505.
9 F. J. M. Hoeben, F. S. Meijer, C. Dekker, S. P. J. Albracht, H. A. Heering and S. G. Lemay, *ACS Nano*, 2008, **2**, 2497–2504.
10 A. Kosari, H. Zandbergen, F. Tichelaar, P. Visser, H. Terryn and A. Mol, *CORROSION*, 2019, **76**, 4–17.
11 J. Liu, B. Wei, J. D. Sloppy, L. Ouyang, C. Ni and D. C. Martin, *ACS Macro Letters*, 2015, **4**, 897–900.
12 W. J. Dearnaley, B. Schleupner, A. C. Varano, N. A. Alden, F. Gonzalez, M. A. Casasanta, B. E. Scharf, M. J. Dukes and D. F. Kelly, *Nano Letters*, 2019, **19**, 6734–6741.
13 J. T. van Omme, H. Wu, H. Sun, A. F. Beker, M. Lemang, R. G. Spruit, S. P. Maddala, A. Rakowski, H. Friedrich, J. P. Patterson and H. H. Pérez Garza, *Journal of Materials Chemistry C*, , DOI:10.1039/D0TC01103G.
14 G. Marchello, C. de Pace, N. Wilkinson, L. Ruiz-Perez and G. Battaglia, *arXiv preprint arXiv:1907.03348:, 2019*.
15 A. Khelfa, C. Byun, J. Nelayah, G. Wang, C. Ricolleau and D. Alloyeau, *Micron*, 2019, **116**, 30–35.
16 S. Keskin, P. Kunnas and N. de Jonge, *Nano Letters*, 2019, **19**, 4608–4613.
17 H. H. Perez-Garza, D. Morsink, J. Xu, M. Sholkina, Y. Pivak, M. Pen, S. van Weperen and Q. Xu, *2016 IEEE 11th Annual International Conference on Nano/Micro Engineered and Molecular Systems (NEMS)*, 2016, 85–90.
18 Z. Liu, C. Shao, B. Jin, Z. Zhang, Y. Zhao, X. Xu and R. Tang, *Nature*, 2019, **574**, 394–398.
19 G.-Z. Zhu, S. Prabhudev, J. Yang, C. M. Gabardo, G. A. Botton and L. Soleymani, *The Journal of Physical Chemistry C*, 2014, **118**, 22111–22119.
20 A. Ianiro, H. Wu, M. M. J. van Rijt, M. P. Vena, A. D. A. Keizer, A. C. C. Esteves, R. Tuinier, H. Friedrich, N. A. J. M. Sommerdijk and J. P. Patterson, *Nature Chemistry*, 2019, **11**, 320–328.
21 N. de Jonge, *Ultramicroscopy*, 2018, **187**, 113–125.
22 N. de Jonge, L. Houben, R. E. Dunin-Borkowski and F. M. Ross, *Nature Reviews Materials*, 2019, **4**, 61–78.
23 K. L. Jungjohann, J. E. Evans, J. A. Aguiar, I. Arslan and N. D. Browning, *Microscopy and Microanalysis*, 2012, **18**, 621–627.
24 J. M. Yuk, J. Park, P. Ercius, K. Kim, D. J. Hellebusch, M. F. Crommie, J. Y. Lee, A. Zettl and A. P. Alivisatos, *Science*, 2012, **336**, 61–64.
25 N. de Jonge and F. M. Ross, *Nature Nanotechnology*, 2011, **6**, 695–704.
26 O. M. Karakulina, A. Demortière, W. Dachraoui, A. M. Abakumov and J. Hadermann, *Nano Letters*, 2018, **18**, 6286–6291.

27 I. Pereiro, A. Fomitcheva Khartchenko, L. Petrini and G. v. Kaigala, *Lab on a Chip*, 2019, **19**, 2296–2314.
28 D. Grujicic and B. Pesic, *Electrochimica Acta*, 2002, **47**, 2901–2912.
29 S. Sarkar, S. Lai and S. Lemay, *Micromachines*, 2016, **7**, 81.
30 J. Zhao, L. Sun, S. Canepa, H. Sun, M. N. Yesibolati, M. Sherburne, R. Xu, T. Sritharan, J. S. C. Loo, J. W. Ager III, J. Barber, K. Mølhave and Z. J. Xu, *J. Mater. Chem. A*, 2017, **5**, 11905–11916.